Geophys. J. Int. (1995) **122**, 675–690

Global phase velocity maps of Love and Rayleigh waves between 40 and 150 seconds

Jeannot Trampert* and John H. Woodhouse
Department of Earth Sciences, Oxford University, 3 Parks Road, Oxford OX1 3PR, *UK*

Accepted 1995 March 7. Received 1995 March 6; in original form 1994 September 20

SUMMARY

Although much is known of the 3-D structure of the Earth, existing models do not make use of much that is known about the large structural perturbations near the surface. It has long been known, for example, that continental and oceanic crustal structures are quite different, and that these differences are evident in the dispersion of Love and Rayleigh waves sampling continental and oceanic paths. Such differences are largest at periods of less than about 100 s. Existing global models do not adequately account for such data, and make allowances for crustal structure in a very approximate way, owing to the incompleteness of information on the global distribution of crustal parameters. As a result, variations in, for example, crustal thickness translate themselves into model artefacts extending to great depth. This can be seen as one aspect of the imperfect resolution of the existing global models. In order to construct higher resolution models of the Earth's outer shell (0–200 km depth), it is necessary to gain more precise knowledge of near-surface structure by incorporating data that have sensitivity to the details of the depth distribution of heterogeneity near the surface. As a first step we analyse a large data set of fundamental-mode Rayleigh and Love waveforms to obtain global phase-velocity maps in the period range 40–150 s. Minor and major arc phase velocities have been determined from about 24 000 digital GDSN and GEOSCOPE seismograms recorded between 1980 and 1990. In order to make such measurements in an automatic way, we have developed a method, using non-linear waveform inversion, in which velocity and amplitude, as a function of frequency, are expanded in B-splines. The waveform data are inverted for the B-spline coefficients, with the application of an explicit smoothness constraint that protects against unwanted effects, such as those due to notches in the amplitude spectra, and avoids some of the problems associated with the phase ambiguity. The cost function (which is minimized in a least-squares sense) presents many local minima, and a good initial model is needed; this is derived by integration of group velocities.

The measurements made using this new technique are then used in a global inversion for phase-velocity distributions of Love and Rayleigh waves, expressed in terms of a spherical harmonic expansion. We show resulting phase-velocity maps up to degree and order 40. These maps are corrected for possible artefacts due to the truncation of the spherical harmonic expansion. We present a detailed resolution analysis which shows that global lateral resolution for surface-wave tomography is of the order of 2000 km. Love-wave phase velocities show a high correlation with known upper mantle structure at long periods and with crustal structure at shorter periods. Similarly, Rayleigh-wave phase velocities correlate well with known tectonic features, but show no clear crustal signature owing to their different sampling of the structure with depth.

Key words: lateral resolution, surface waves, tomography.

* Now at: EOPGS, 5 Rue René Descartes, F-67084 Strasbourg, France.

1 INTRODUCTION

The dispersive properties of surface waves have been used to infer the Earth's internal structure since the early twenties. Gutenberg (1924), using data collected by Tams (1921), explained the dispersion differences between surface waves propagating along oceanic and continental paths in terms of properties of the Earth's crust. Throughout the next few decades, many scientists studied different parts of the world and produced average regional models based on surface-wave data. The important crustal types (shield, mid-continent, etc) that have emerged from surface-wave studies are summarized in Brune (1969). Similarly, Dorman (1969) reviews different regional upper-mantle models derived from surface waves. More recently, much work has been done at very long periods, leading to rather precise knowledge of the global distribution of phase velocities at periods greater than about 150 s, for low degrees in the spherical harmonic expansion of heterogeneity. For example, by measuring the shifts in spectral peaks, Masters *et al.* (1982) discovered a strong pattern of degree 2 in the phase velocities of Rayleigh waves at periods greater than 200 s. Nakanishi & Anderson (1982, 1983, 1984) made expansions up to degree 6 using measurements of group and phase velocities. Woodhouse & Dziewonski (1984) introduced a technique of waveform inversion in which the direct measurement of group and phase velocities was avoided; nevertheless, since the largest features in their data set were the fundamental-mode Rayleigh and Love orbits, their models accurately represent the distribution of phase velocities at periods greater than about 150 s. Wong (1989) measured phase and amplitude anomalies by a deconvolution procedure, using synthetic seismograms, and constructed phase-velocity maps up to degree 12 for Rayleigh and Love waves in the period range 150–300 s. Here we adopt a similar approach, but seek to apply it at shorter periods (40–150 s), overlapping with those used in the early studies which first identified strong regional differences.

The aim of this paper is to produce phase-velocity maps at frequencies sensitive to the structure of the crust and uppermost mantle and to assess the lateral resolution achievable with modern surface-wave coverage. The great wealth of available digital seismograms demands new ways of processing. It is now possible to have all these data online, and our concern has been to design an automatic analysis procedure. We will describe a new non-linear waveform inversion for amplitude and phase velocity as a function of frequency. Special care will be taken to describe the usefulness of the explicit smoothness constraint that we apply. We show that the additional introduction of group-velocity information allows the algorithm to be automated. We briefly describe the data used and the construction of global phase-velocity maps expanded on a spherical harmonic basis. Special care has been taken to avoid possible artefacts resulting from the truncation of the expansion. Finally, we present a detailed resolution analysis and briefly discuss the results and compare them with previous work.

2 PHASE-VELOCITY MEASUREMENTS

We propose a new approach to waveform inversion, which directly inverts the relevant part of the seismogram for amplitude and phase anomalies with respect to a reference model. The approach is general and may be applied to single-station, two-station or great-circle paths.

2.1 Waveform inversion

Let $D(\omega)$ be the Fourier transform of the normalized observed seismogram supposed to contain a fundamental surface-wave mode only, and $S(\omega)$ the corresponding fundamental-mode synthetic seismogram computed for a given earth model. Normalization is performed by dividing each seismogram by its rms amplitude. We may write

$$D(\omega) = A(\omega) \exp[-i\omega\Delta\delta s(\omega)]S(\omega), \tag{1}$$

where $A(\omega)$ denotes the amplitude correction and $\delta s(\omega)$ the phase slowness perturbation with respect to the earth model employed. Δ is the station–event distance and ω the angular frequency. We expand amplitude and phase in terms of cubic B-splines (e.g. Lancaster & Salkauskas 1986):

$$A(\omega) = \sum_{i=1}^{N} \alpha_i B_i(\omega), \tag{2}$$

$$\delta s(\omega) = \sum_{i=1}^{M} \beta_i B_i(\omega), \tag{3}$$

with $B_i(\omega)$ the ith cubic B-spline and α_i and β_i constants to be found. In the following, we will drop the explicit frequency dependence of $D(\omega)$, $S(\omega)$, $A(\omega)$, $\delta s(\omega)$ and $B_i(\omega)$ in our notation. Eq. (1) contains both real and imaginary terms, and we can write the following amplitude equation, completely decoupled from the phase terms:

$$|D| = A\,|S| \equiv f(\omega, \alpha_i). \tag{4}$$

Eq. (4) defines a simple linear inverse problem for the coefficients α_i defined in (2), where the partial derivatives are given by

$$\frac{\partial f(\omega)}{\partial \alpha_i} = B_i\,|S|. \tag{5}$$

Similarly, from (1) we obtain two phase-velocity equations:

$$\mathcal{Re}(D) = A[\mathcal{Re}(S)\cos(\omega\Delta\delta s) + \mathcal{Im}(S)\sin(\omega\Delta\delta s)] \equiv g(\omega, \beta_i), \tag{6}$$

$$\mathcal{Im}(D) = A[\mathcal{Im}(S)\cos(\omega\Delta\delta s) - \mathcal{Re}(S)\sin(\omega\Delta\delta s)] \equiv h(\omega, \beta_i), \tag{7}$$

In contrast to eq. (4), expressions (6) and (7) define a non-linear inverse problem for the coefficients β_i, with the α_i known. This problem will be solved iteratively, and after each step the partial derivatives are updated using

$$\frac{\partial g(\omega)}{\partial \beta_i} = A[-\omega\Delta B_i\,\mathcal{Re}(S)\sin(\omega\Delta\delta s) + \omega\Delta B_i\,\mathcal{Im}(S)\cos(\omega\Delta\delta s)], \tag{8}$$

$$\frac{\partial h(\omega)}{\partial \beta_i} = A[-\omega\Delta B_i\,\mathcal{Im}(S)\sin(\omega\Delta\delta s) - \omega\Delta B_i\,\mathcal{Re}(S)\cos(\omega\Delta\delta s)]. \tag{9}$$

The inverse problem for the phase coefficients β_i is highly non-linear, particularly at higher frequencies, and its solution is dependent on the starting model. In order for it to converge uniquely to the final solution, some other information is needed. We have chosen to introduce group-velocity measurements, which are secondary observables easily calculated from the seismograms. Knowing that

$$U(\omega) = \frac{c(\omega)}{1 - \omega c'(\omega)/c(\omega)}, \tag{10}$$

where $U(\omega)$ and $c(\omega)$ are group and phase velocities, respectively, and $[']$ denotes the derivative with respect to ω, it is straightforward to show that the group slowness perturbation is given by

$$\delta\left(\frac{1}{U}\right) = \delta s + \omega \delta s' \equiv k(\omega, \beta_i). \tag{11}$$

In contrast to (6) and (7), this equation corresponds to a linear inverse problem for the coefficients β_i defined in (3) with the following partial derivatives:

$$\frac{\partial k(\omega)}{\partial \beta_i} = B_i + \omega B_i'. \tag{12}$$

Our inverse problem for amplitude correction and phase slowness perturbation is now completely defined, and will be solved with a standard least-squares algorithm (Tarantola & Valette 1982). The data are related to the model by $\mathbf{d} = \boldsymbol{\gamma}(\mathbf{m})$ and the estimated model $\mathbf{m}$ minimizes the cost function

$$\boldsymbol{\Phi}(\mathbf{m}) = [\mathbf{d} - \boldsymbol{\gamma}(\mathbf{m})]^{\mathrm{T}}\mathbf{C}_{\mathrm{d}}^{-1}[\mathbf{d} - \boldsymbol{\gamma}(\mathbf{m})] + \mathbf{m}^{\mathrm{T}}\mathbf{C}_{\mathrm{m}}^{-1}\mathbf{m}, \tag{13}$$

which expresses the classical trade-off between data fit and minimum model norm. Matrices $\mathbf{C}_{\mathrm{d}}$ and $\mathbf{C}_{\mathrm{m}}$, the *a priori* covariance matrices of data and model, quantify the expected data variance and model norm. The specification of the covariance matrices will be described below. Matrix $\mathbf{C}_{\mathrm{m}}$ will be chosen to apply smoothing to the solution as a function of frequency. The solution is sought iteratively using the algorithm

$$\begin{aligned}\mathbf{m}_{i+1} &= \mathbf{m}_0 + (\mathbf{G}^{\mathrm{T}}\mathbf{C}_{\mathrm{d}}^{-1}\mathbf{G} + \mathbf{C}_{\mathrm{m}}^{-1})^{-1} \\ &\quad \times \mathbf{G}^{\mathrm{T}}\mathbf{C}_{\mathrm{d}}^{-1}[(\mathbf{d} - \boldsymbol{\gamma}(\mathbf{m}_i)) + \mathbf{G}(\mathbf{m}_i - \mathbf{m}_0)].\end{aligned} \tag{14}$$

The algorithm (14) may be applied to linear as well as to non-linear sets of equations. For a linear problem, (14) will converge in one iteration. This applies to expressions (4) and (11), whereas the solution of the non-linear equations (6) and (7) needs multiple iterations. The practical implementation of the algorithm is further described below.

2.2 *A priori* information

Dispersion curves are intrinsically smooth. The effects of lateral and vertical heterogeneities are averaged during surface-wave propagation, depending on distance and frequency, respectively. From a physical point of view it is reasonable, therefore, to introduce a smoothness constraint into the inversion algorithm. We require the roughness of the model to be minimum. The roughness of a function $m(\omega)$ may be defined as

$$R = \int_{\omega_1}^{\omega_N} \left[\frac{d^2 m(\omega)}{d\omega^2}\right]^2 d\omega, \tag{15}$$

where the function $m(\omega)$ is twice continuously differentiable between ω_1 and ω_N. Our model is expanded on a B-spline basis whose elements are twice continuously differentiable, and we obtain

$$R = \int_{\omega_1}^{\omega_N} \left[\sum_{i=1}^{N} \epsilon_i \frac{d^2 B_i(\omega)}{d\omega^2}\right]^2 d\omega \tag{16}$$

or, in matrix form,

$$\mathbf{R} = \boldsymbol{\epsilon}^{\mathrm{T}}\mathbf{H}\boldsymbol{\epsilon}, \tag{17}$$

where

$$H_{ij} = \int_{\omega_1}^{\omega_N} \frac{d^2 B_i(\omega)}{d\omega^2}\frac{d^2 B_j(\omega)}{d\omega^2} d\omega.$$

We shall write

$$\mathbf{C}_{\mathrm{m}}^{-1} = \lambda \mathbf{H}, \tag{18}$$

where λ (>0) plays the role of a smoothing parameter controlling the trade-off between roughness and fit to the data. $\mathbf{C}_{\mathrm{m}}^{-1}$ is band-diagonal and allows very efficient calculations. This approach is closely related to that of Constable & Parker (1988), where the practical implementation of B-splines and regularization with smoothing splines is described in detail. The above development shows how to introduce an explicit smoothness constraint in a least-squares inversion using algorithm (14). Because the data have been normalized prior to inversion, $\mathbf{C}_{\mathrm{d}}^{-1}$ is chosen equal to the identity matrix, the magnitude of the data variance being absorbed in the parameter λ.

In addition to having a physical meaning, we will explain how this smoothness constraint has practical advantages in our measurements, avoiding problems related to notches in the spectrum and the phase ambiguity.

2.3 Automatic algorithm

The waveform inversion for amplitude and phase velocity as a function of frequency is completely automatic. This means that at no stage does an operator have to interact in the process to make a decision (e.g. data too noisy, poor final data fit). To make sure that the final result corresponds to correct measurements, a number of safe-guards need to be built into the algorithm. The methodology used in this paper is motivated by surface ray theory, and some consequences of this approach are discussed in Section 5.

(1) The waveform to be inverted consists of fundamental-mode surface waves cut from the complete seismogram using a group-velocity window. We consider as noise that portion of the seismogram before the start of the fundamental-mode surface wave. This noise signal is also defined by a group-velocity window. We compute the maximum amplitudes of the envelope of the noise signal and the total signal. The fundamental surface waveform is considered to be pure if the signal-to-noise ratio is above a certain threshold, which we fixed to be 7. This simple consideration is very effective in detecting higher mode and S-wave interference, or poorly excited surface waves for deep and/or small events. Approximately 60 per cent of all considered waveforms are rejected with this criterion. We considered data from magnitude 5.5 onwards and most of the rejected data correspond to magnitudes below 5.9. Above magnitude 5.9, rejections were almost exclusively of waveforms corresponding to major arcs.

(2) In order to obtain the phase velocity, it would be

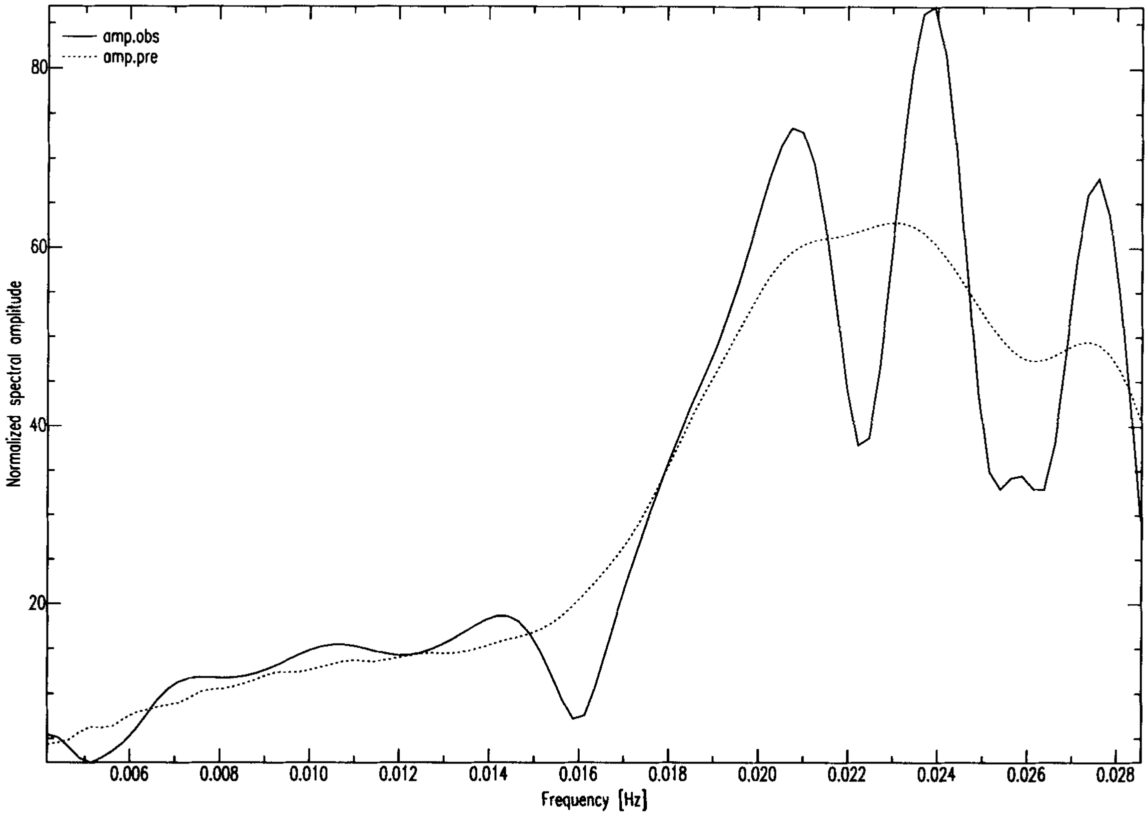

Figure 1. Observed (solid line) and predicted (dotted line) amplitude spectrum of a Love wave recorded at station CRZF at a distance of 16 378 km from the epicentre. The event has a magnitude of 5.8 and the reference 010590D in the Harvard CMT catalogue. The observed spectrum clearly shows 4 notches, which have been interpolated during the inversion. The variance reduction of only 80 per cent indicates the presence of notches.

sufficient to introduce the spectral ratio of the observed to the synthetic signal at each frequency into eqs (6) and (7). Instead, we have chosen to invert eq. (4) for the coefficients α_i of the B-spline expansion of the amplitude correction. With the constraint (18), we recover a smooth interpolation of the spectral ratio of the observed over the synthetic signal. We fixed $\lambda = 10^{-6}$, which means that priority is nevertheless given to fitting the data. This weak requirement of smoothness is effective in interpolating through notches in the observed spectrum, where the phase may be poorly defined. Below a certain threshold of variance reduction, which we fixed to be 85 per cent, there is a high probability that such notches occur and we reject the data. Consider the example in Fig. 1, where we see 4 notches in the spectrum. The variance reduction is 80 per cent in this case, and the seismogram is rejected. Allowing a phase-velocity determination for this example showed that it is not possible to fit the phase at periods near 180 s. Many other factors may affect amplitude measurements. We believe that, with a correct instrument response and correct source parameters, spherical earth models should allow amplitudes to be predicted to within a factor 3, at least at long periods, and we elected to reject all seismograms where amplitude predictions vary by more than a factor 3 at any given frequency with respect to the observed data. The aim of this rather conservative criterion is to select data for which the source parameters are well known and for which departures from ray theory are not too large. About 25 per cent of all considered waveforms did not pass this amplitude test and were eliminated; the number of rejected seismograms is a decreasing function of earthquake magnitude. Among the possible causes for such poor amplitude agreement are (i) inaccurate source parameters, (ii) focusing, defocusing and off-path propagation due to lateral refraction, (iii) multipathing, and (iv) departures from ray theory. A recent study by Friederich *et al.* (1994) has shown that such effects can be large, particularly for frequencies somewhat higher than those used in the current study. All such effects will be particularly significant near nodes in the surface-wave radiation patterns, and the amplitude test has the desirable effect of eliminating such paths from further analysis.

(3) The inversion of eqs (6) and (7) is a highly non-linear problem for the coefficients β_i corresponding to the B-spline expansion of δs. The cost function has many local minima and the solution is dependent on the starting model. We have chosen to integrate the group velocity, a secondary observable readily calculated from the observed seismogram, to obtain a starting model compatible with the same original waveform. At this stage, any data with a group-velocity perturbation greater than 10 per cent with respect to the chosen earth model are eliminated. In practice, this involves solving (11) for the initial B-spline coefficients of the phase slowness perturbation. This problem is linear and straightforward. Again we have given priority to the data fit and used $\lambda = 10^{-6}$ in (18).

(4) Starting with the model calculated from the group

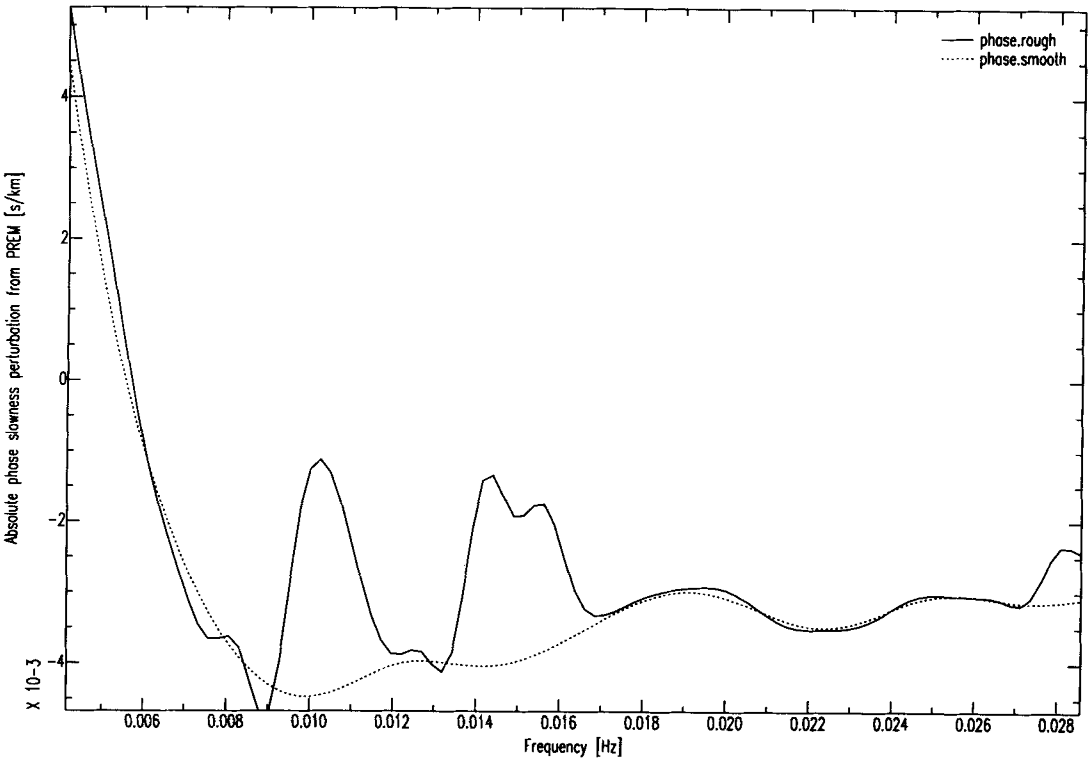

Figure 2. Undamped (solid line) and smooth (dotted line) phase-velocity determination from a major-arc Rayleigh wave recorded at station DRV. The distance is 27 095 km, and the event is the same as for Fig. 1. The undamped solution presents 2π-jumps at periods 100 and 65 s. The smoothness constraint correctly eliminates these jumps.

velocity, the solution converges to the absolute minimum of the cost function. Even with a good starting model, eqs (6) and (7) are so rapidly varying in δs that the probability of divergence of the algorithm is not negligible. We simply added the group-velocity data to the system again to act as linear constraints (with a relative weight 10^{-5} of the phase data). This means that our final phase velocities are compatible with the phase of the original seismograms as well as with the measured group velocities.

(5) The last problem to overcome is due to the fundamental phase ambiguity in the seismograms arising from the multivalued nature of the Fourier phase. If we gain a complete cycle in phase, the corresponding phase slowness changes by $2\pi/\omega\Delta$. The nature of the inverse problem is such that the solution stays as close as possible to the initial model. The result is jumps of $2\pi/\omega\Delta$ in the final slowness perturbation. If we require the slowness perturbation to be sufficiently smooth, such jumps are not allowed, and the solution follows the correct number of cycles in the phase. Note that exactly the same is done manually, where the integer arising from the multivalued Fourier phase is determined so that the measured phase velocity connects smoothly from period to period. Fig. 2 clearly shows the effect of the smoothness constraint. We used $\lambda = 10^{-2}$, which is sufficient to avoid jumps of $2\pi/\omega\Delta$. We require that the data variance reduction reaches at least 85 per cent and that at no frequency is the perturbation higher than 10 per cent with respect to the earth model. Finally, we make a global $2\pi/\omega\Delta$ shift, so that the phase velocity is closest to that of the spherical earth model at a period of 150 s.

The amplitude and phase-velocity measurements are set up as a non-linear waveform inversion and are completely independent of an interactive operator. The algorithm depends on a few parameters which have been carefully tuned from the manual analysis of numerous seismograms. Some of the selection criteria are very conservative. They have been chosen with the aim of having well-excited, purely fundamental-mode, surface waves at all frequencies considered, and reasonable corresponding source parameters. The data fit for a finally selected waveform is best seen in Fig. 3, where we have randomly chosen a seismogram and compared it with the predicted seismogram after inversion. Besides the representation of the complete waveforms, the observed and predicted seismograms have been narrowband-filtered at periods of 150, 80 and 40 s and show a good fit for each frequency band.

3 DATA

The raw data set consists of long-period Love and Rayleigh waves. We considered all digital data available from the GDSN and GEOSCOPE networks recorded between 1980 and 1990. We selected data for events with a magnitude greater than 5.5. The minimum distance between station and event was set to 20° to avoid possible interferences between S waves and surface waves as well as near-field effects. The maximum allowed distance was chosen to be 160° to avoid possible interferences between minor- and major-arc waves. Seismograms have been rotated to radial and transverse components and resampled at 1 point every 16 s. Love

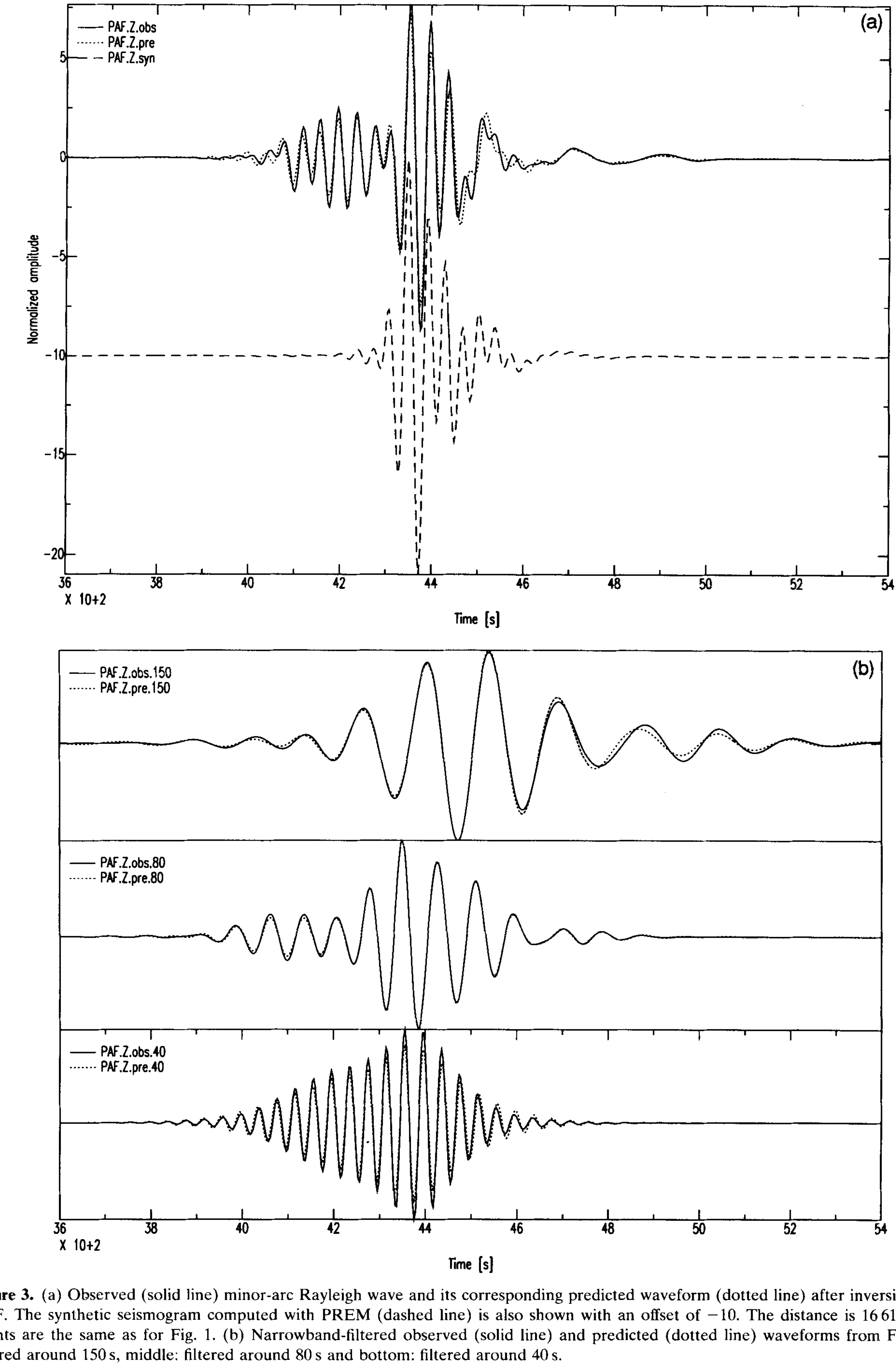

Figure 3. (a) Observed (solid line) minor-arc Rayleigh wave and its corresponding predicted waveform (dotted line) after inversion for station PAF. The synthetic seismogram computed with PREM (dashed line) is also shown with an offset of −10. The distance is 16 610 km and the events are the same as for Fig. 1. (b) Narrowband-filtered observed (solid line) and predicted (dotted line) waveforms from Fig. 3(a). Top: filtered around 150 s, middle: filtered around 80 s and bottom: filtered around 40 s.

waves are measured on transverse components, and Rayleigh waves on vertical components.

Each observed seismogram was time-variable filtered (Cara 1973) using the group velocity corresponding to PREM (Dziewonski & Anderson 1981). The time interval around the group arrival time was chosen to be sufficiently large as to avoid any loss of energy in the observed surface wave, which was reconstructed between periods of 35 and 250 s. Corresponding to each observed seismogram, we computed a synthetic seismogram using normal-mode summation (Gilbert 1971; Dziewonski & Woodhouse 1983). The source parameters (origin time, source duration, depth and moment tensor) were taken from the Harvard catalogue. Latitude and longitude were taken from the NEIS or the ISC catalogue, since we anticipate that, while depth estimates from long-period waveforms improve upon those determined from arrival-time data, the epicentral locations probably do not (Dziewonski & Woodhouse 1982). We assumed the source parameters to be correct and did not allow for any perturbations in the inversion scheme. The synthetics were calculated using the Preliminary Reference Earth Model (PREM; Dziewonski & Anderson 1981). An ellipticity correction was introduced at this stage, and the instrument response of the observed seismogram was applied. We cut the seismograms with group-velocity windows of 5.3–3.3 km s^{-1} and 4.8–3.0 km s^{-1} for Love and Rayleigh waves, respectively. The noise signal, referred to above, was defined by the group-velocity windows of 5.3–4.8 km s^{-1} and 4.8–4.4 km s^{-1} for Love and Rayleigh waves, respectively.

As mentioned before, the waveform inversion is completely automatic. A number of safe-guards are built into the algorithm. If all the required conditions described in the previous paragraphs are fulfilled, the measurement is deemed satisfactory and included in the final inversions.

The number of paths surviving these tests, including minor and major arcs, was approximately 24 000 (10 000 for Love and 14 000 for Rayleigh waves). This corresponds to about 10 per cent of all considered waveforms. All seismograms are treated in exactly the same way, with the same explicit *a priori* information resulting in the most homogeneous phase-velocity and amplitude data set to date. The precise coverage is summarized in Table 1. A map of great-circle path coverage would show all parts of the Earth sampled, with GDSN data mainly covering the American, Eurasian and Pacific plates, and GEOSCOPE data mainly covering the African, Indo-Australian and Antarctic plates. Although the data coverage is excellent in this study, it is not homogeneous owing to the distribution of earthquakes and stations.

Table 1. Total number of great-circle paths used in this study. The data have been selected from the GDSN and GEOSCOPE networks using both, LH and VH, channels and correspond to events with a magnitude greater than 5.5 in the considered time span. In 1990, we only had access to data recorded between January and July.

Year	Number of events	Number of rays			
		G_1	G_2	R_1	R_2
1980	231	567	11	653	89
1981	236	532	13	536	64
1982	229	643	19	652	67
1983	290	1067	44	952	149
1984	243	752	27	767	122
1985	247	906	34	941	127
1986	249	924	31	893	144
1987	274	1192	51	1582	170
1988	260	1047	52	1672	168
1989	259	1252	57	2406	224
1990	166	758		1470	
Total	2684	9640	339	12524	1324

4 GLOBAL PHASE-VELOCITY MAPS

4.1 Inversion for phase-velocity distributions

We made average phase-velocity measurements over minor and major arcs relative to the PREM phase velocities. Explicitly, we may write for one given frequency that

$$d_i = \int G_i(\theta, \varphi) \frac{\delta c(\theta, \varphi)}{c} d\Omega \tag{19}$$

where d_i is the ith measurement, θ and φ are colatitude and longitude, respectively, G_i are the data kernels, $\delta c(\theta, \omega)/c$ is the true relative phase-velocity perturbation, and the integration is over the sphere representing the earth. In the general case, the data kernels describe the true sampling of the earth by the surface wave. In the present study, we assume the validity of the great-circle approximation, which means that G_i is zero everywhere except along the minor and major arcs. Producing a phase-velocity map from such measurements is then a simple interpolation problem, where we have chosen to expand the relative phase-velocity perturbations in a spherical harmonic basis:

$$\frac{\delta c}{c} = \sum_{l=0}^{L} \sum_{m=-l}^{l} \xi_{lm} Y_{lm}(\theta, \varphi), \tag{20}$$

where l is the degree and m the order of the spherical harmonic Y_{lm}. This leads to a simple least-squares inversion for the coefficients ξ_{lm} to be solved with eq. (14), where the derivatives are the integrals of the spherical harmonics along the minor and major arcs. Following the ideas of Shure, Parker & Backus (1982) and Parker (1994), we wish to retrieve a smooth model and define the roughness of the model over the sphere as

$$R = \int \left[\sum_{l=0}^{L} \sum_{m=-l}^{l} \xi_{lm} \nabla_S^2 Y_{lm} \right]^2 d\Omega, \tag{21}$$

where ∇_S^2 denotes the surface Laplacian. Requiring the roughness of the model to be minimum, and using the normalization convention of Edmonds (1960), similar arguments to those in Section 2.2 lead to a diagonal *a priori* model covariance matrix given by

$$(C_m^{-1})_{jj} = \lambda [l(l+1)]^2, \tag{22}$$

where j is the index numbering the $(L+1)^2$ coefficients and l is the degree of the corresponding spherical harmonic. λ (>0) again is a smoothing parameter controlling the trade-off between roughness and fit to the data. Note that the model covariance depends only on the degree of the spherical harmonic and not on its order. In other words, all coefficients corresponding to the same spherical harmonic degree are equally weighted.

To describe the Earth's structure fully, the set of spherical harmonics must be complete, and hence the summation in (20) has to be carried out to infinity. This would lead to an ill-posed inverse problem. In practice, we are limited by the finite resolution of the data, so that we have to choose an upper limit L. The result of truncating the expansion is to lead to a long-wavelength estimation of the true Earth, where the maximum lateral resolution is given by the highest degree considered. This looks like a very attractive way of finding a smooth approximation to the true Earth, but there is a hidden catch which may bias the retrieved model.

This problem is related to ringing, as described in detail in a spherical harmonic analysis of the geomagnetic field by Whaler & Gubbins (1981). They showed that truncating the spherical harmonic expansion generates side lobes in the averaging kernels (Backus & Gilbert 1968) with a particular prominent peak at the antipodes. This is analogous to Fourier filtering. Truncating a Fourier spectrum with a straight cut-off is well known to give ringing, and the same applies to the spherical case. The remedy in Fourier analyses is to taper the form of the cut-off, and Whaler & Gubbins (1981) suggested the same in spherical harmonic analyses. They progressively down-weighted coefficients corresponding to higher and higher spherical harmonic degrees. A close inspection of (22) shows that our *a priori* model covariance does exactly the same: the higher the spherical harmonic degree, the higher the damping of the corresponding coefficients. An explicit smoothness constraint is thus a natural way of reducing ringing.

The introduction of a smoothness constraint is thus effective against possible artefacts due to ringing in least-squares interpolation problems using model expansions on incomplete sets of basis functions. We should, however, not hide a drawback inherent to this approach, namely a trade-off between bias reduction and lateral resolution. Because we down-weight, or damp, coefficients corresponding to higher and higher degrees, we have to expect that we will not be able to retrieve completely the earth's structure corresponding to the highest degrees in our expansion. The effective resolution should thus be expected to be lower than suggested by the maximum degree L. We will discuss this in greater detail in the following section. Another important point is that the smoothness constraint (as well as any other form of damping for that matter) imposes an *a priori* shape upon the high-degree power spectrum, independently of any structural information. This should be kept in mind when relating the power spectra of models to the nature of the Earth's structure.

Our final models are the spherical harmonic expansions, to degree and order 40, of Love- and Rayleigh-wave phase-velocity perturbations for the period range 40–150 s. As an example, results at 40 s period are tabulated in the Appendix. A complete set of numerical coefficients is available from the authors on request. Figs 4 and 5 show the relative phase-velocity perturbations of Love and Rayleigh waves at 40, 80 and 150 s.

4.2 Resolution

Algorithm (14) used to infer the spherical harmonic coefficients for the phase-velocity maps allows a complete resolution analysis. The resolution matrix obtained from (14) applies to the coefficients itself, and its interpretation is not straightforward. We prefer to convert the resolution matrix into averaging kernels (Backus & Gilbert 1968) given by

$$\frac{\delta c(\theta_0, \varphi_0)}{c} = \int A(\theta, \varphi; \theta_0, \varphi_0) \frac{dc(\theta, \varphi)}{c} d\Omega. \tag{23}$$

The above equation states that the relative phase velocity estimated at position (θ_0, φ_0) is an average of the true model over the whole Earth with weights $A(\theta, \varphi; \theta_0, \varphi_0)$, the averaging kernels. The rotation of the resolution matrix into the relative phase-velocity space is trivial and A is readily calculated. Fig. 6 shows an example of an averaging kernel, which ideally should be a Dirac function. In our case, it is a peaked function at the central point, with no prominent side lobes, as expected because we suppressed ringing. To give a complete picture of the resolution we would need to show such kernels for each point on the Earth's surface. As most of the area over which the true model is averaged is contained in the central peak, we have chosen to represent the radius of the central peak only. Maps of resolving radii are shown in Fig. (7) for Love and Rayleigh waves. They are dependent only upon the path coverage and the smoothness parameter λ and give a good representation of the lateral resolution that can be achieved. There is a very high correlation between resolving radii and ray density (high lateral resolution corresponds to dense path coverage and vice versa), but resolving radii give further quantitative information on the extent of lateral resolution.

In general, lateral resolution is higher for Rayleigh waves than for Love waves. This is particularly evident in the Southern hemisphere for which most stations are located on islands where the horizontal noise level is on average 10 times higher than vertical macroseismic noise. This results in a lower ray-path coverage for Love waves than for Rayleigh waves. The highest lateral resolution between 1000 and 1700 km, which corresponds to spherical harmonic degrees of 40–23, is achieved only in some areas of the globe, principally the Western Pacific and North America. Other parts of the world have resolving lengths between 1700 and 2400 km (degrees 23–16). For Love waves, resolution in the Southern hemisphere may go down to degrees 12–6 in some areas. The trace of the resolution matrix gives the number of independently resolved parameters, and hence also the average lateral resolution. For Rayleigh waves the trace is 642, which suggests an average resolution of degree 24, and for Love waves the trace is 529, corresponding to a resolution of degree 22, which correlates well with the average resolution obtained from the resolving radii. The resolving radii are dependent on the smoothing parameter λ. The maps shown in Fig. 7 are obtained for $\lambda = 10^{-4}$. If we increase the smoothing parameter, the resolving radius will

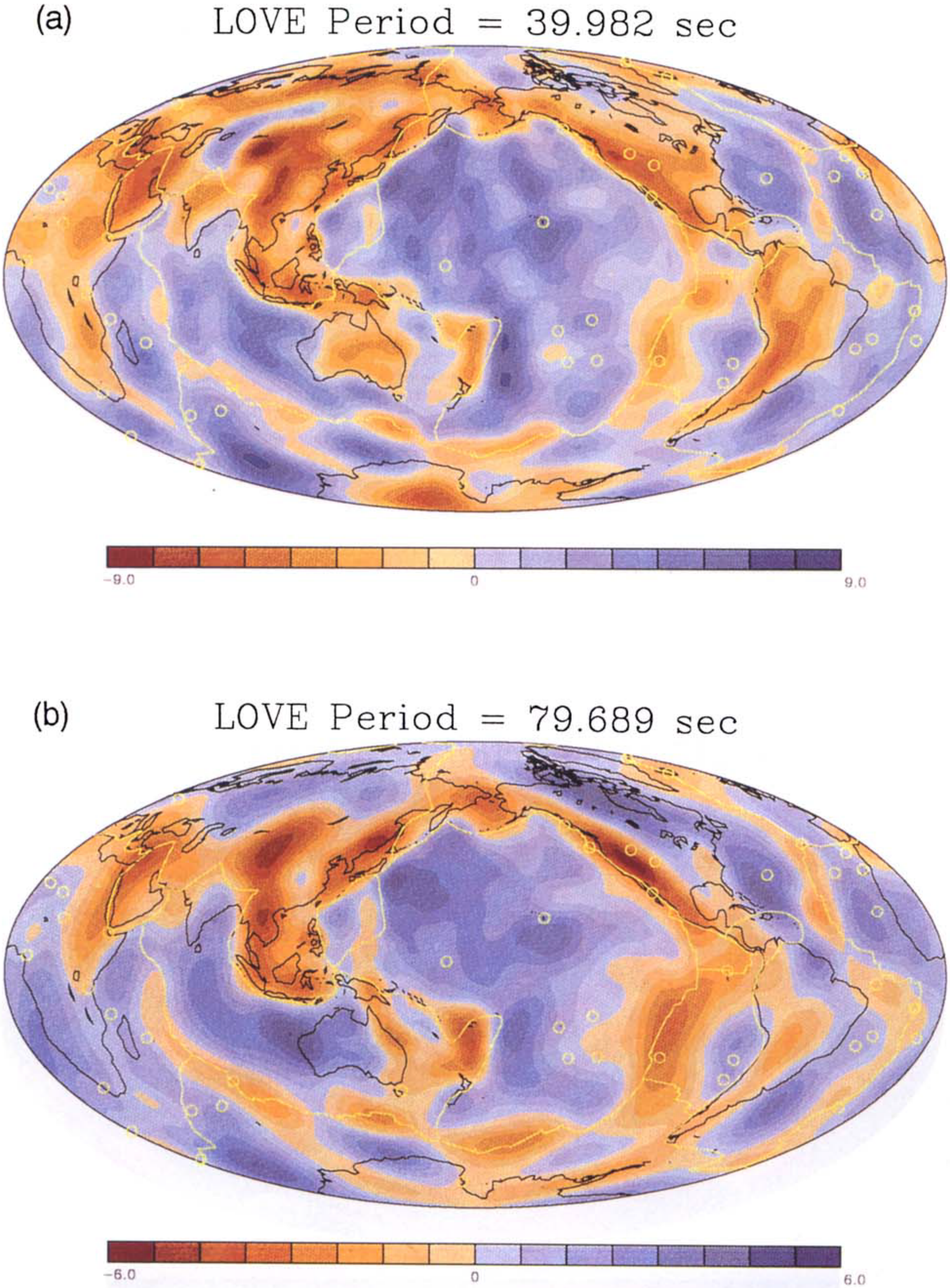

Figure 4. (a) Love-wave phase-velocity perturbation at a period of 39.982 s. The variations are given in per cent with respect to the PREM average. Yellow lines are plate boundaries, and yellow circles are hotspots. The smoothness parameter $\lambda = 10^{-4}$. (b) As for (a), but for a period of 79.689 s and $\lambda = 5 \times 10^{-4}$. (c) As for (a) but for a period of 150.919 s and $\lambda = 10^{-3}$.

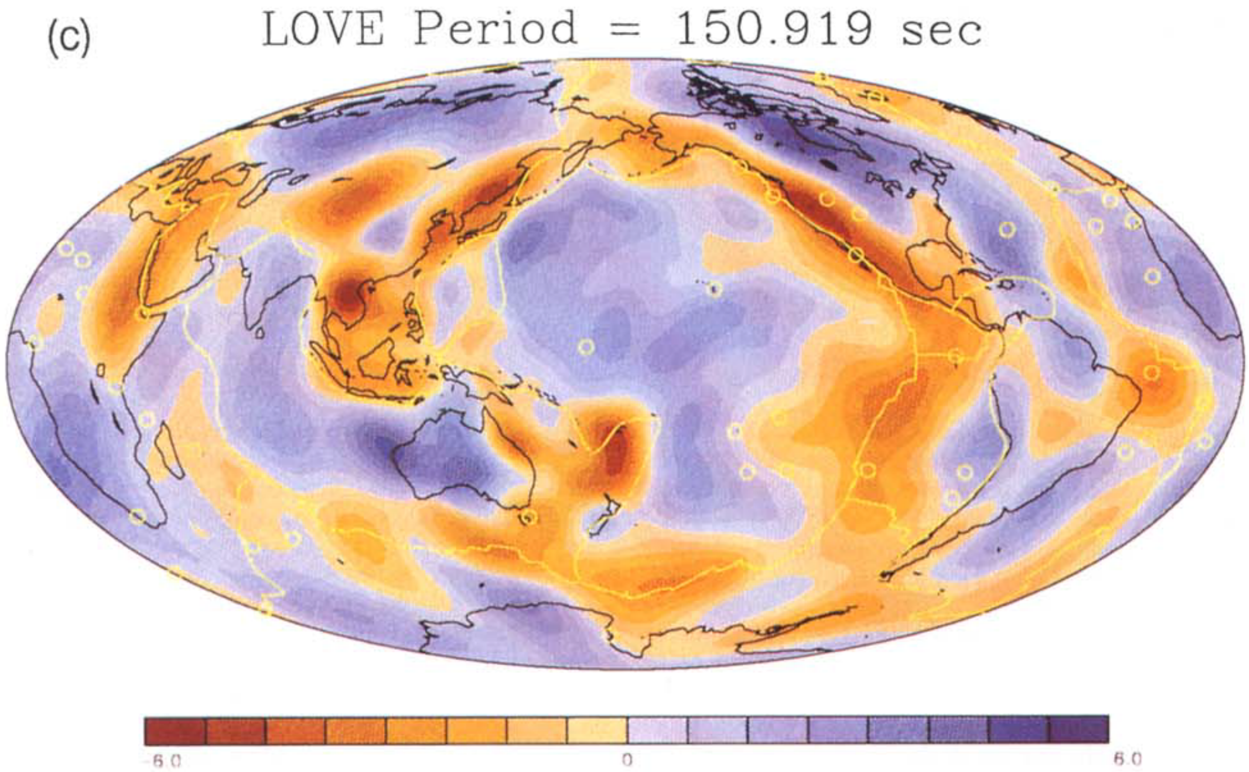

Figure 4. (*Continued.*)

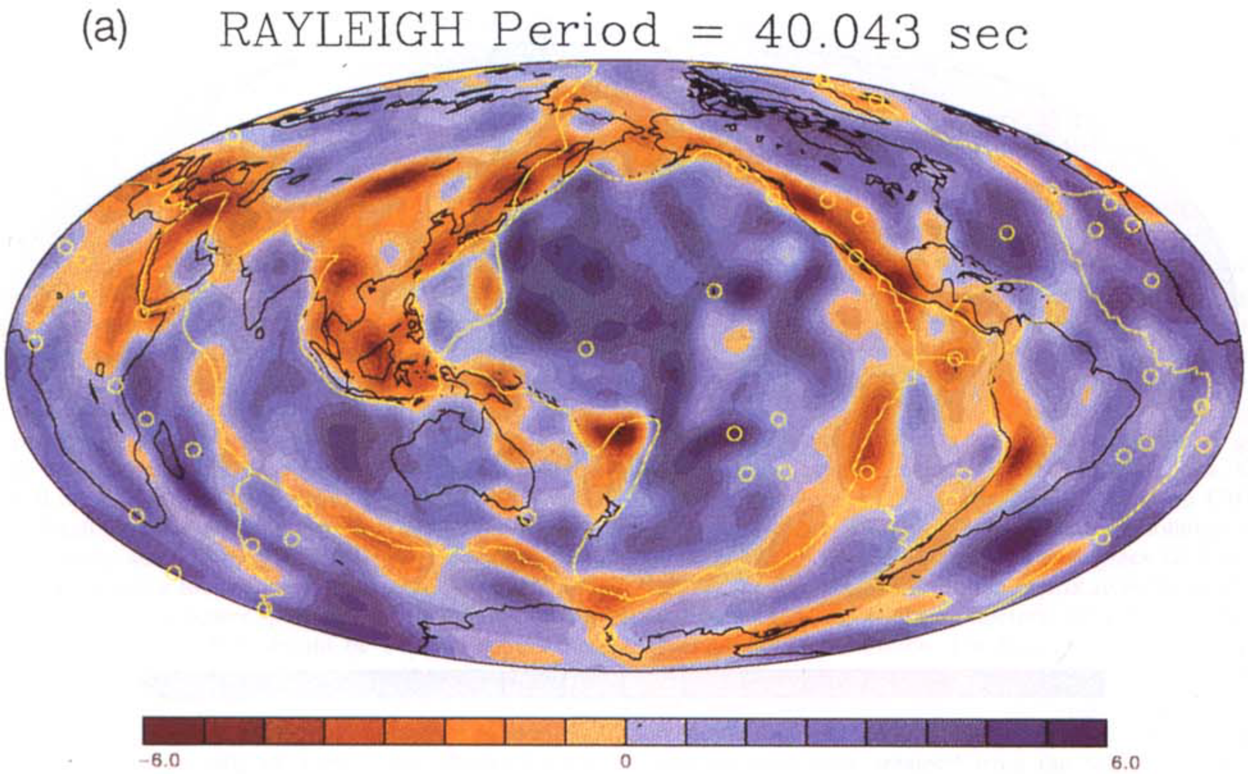

Figure 5. As for Fig. 4(a), but for a Rayleigh wave at a period of 40.043 s and $\lambda = 10^{-4}$. (b) As for Fig. 4(a), but for a Rayleigh wave at a period of 79.909 s and $\lambda = 5 \times 10^{-4}$. (c) As for Fig. 4(a), but for a Rayleigh wave at a period of 149.124 s and $\lambda = 10^{-3}$.

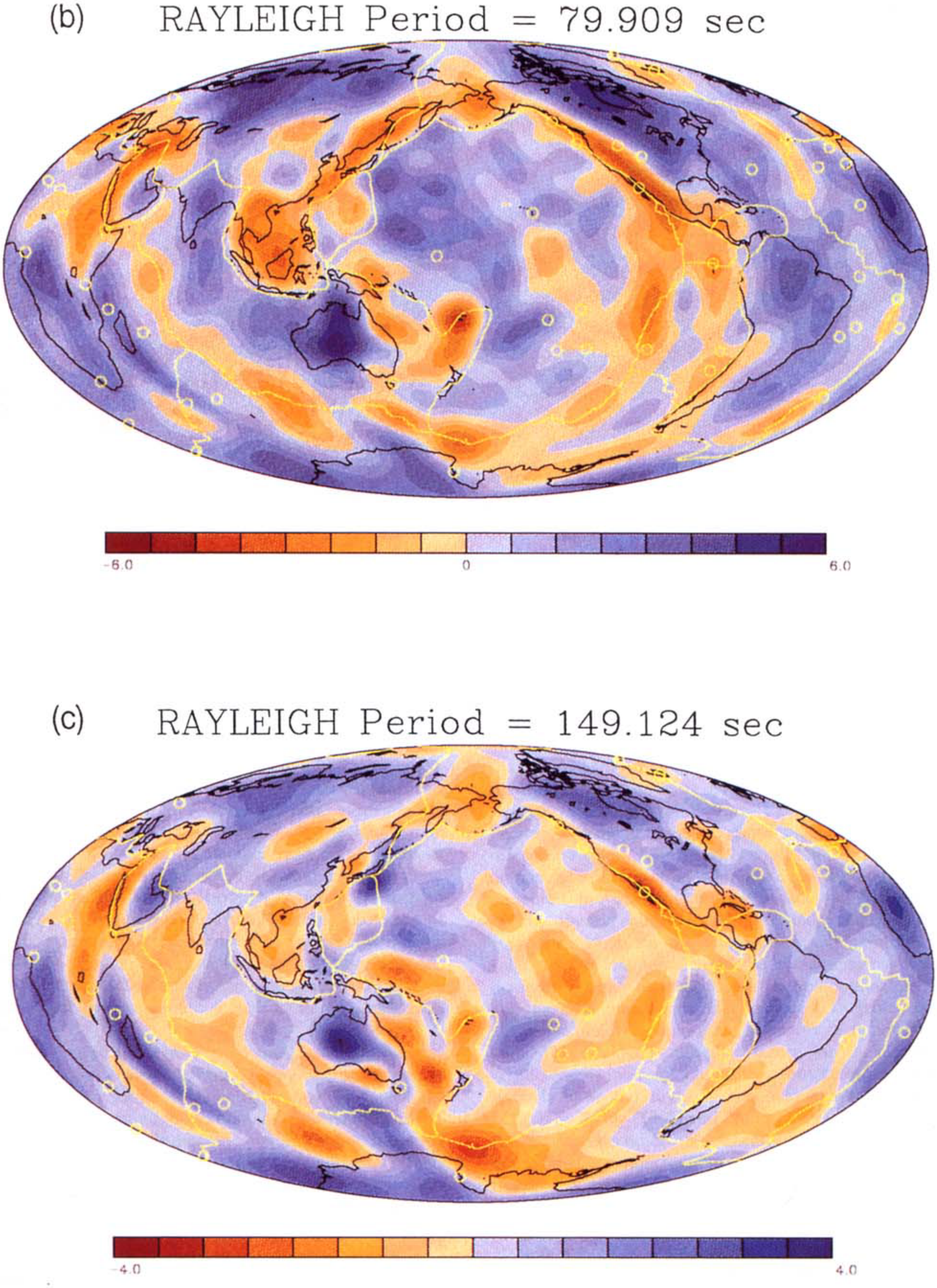

Figure 5. (*Continued*.)

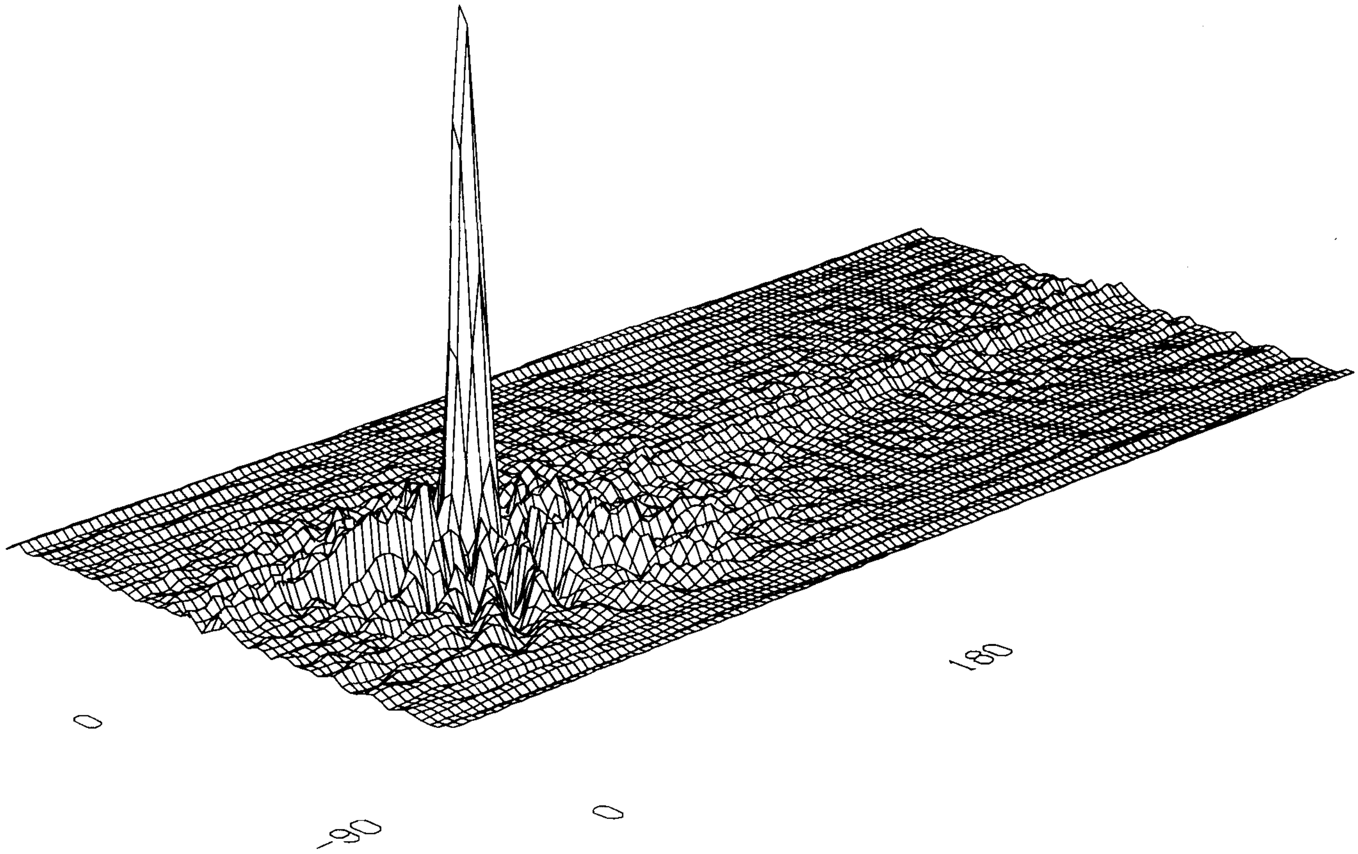

Figure 6. Averaging kernel at latitude = 0° and longitude = 90° corresponding to the Rayleigh-wave path coverage and a smoothness parameter $\lambda = 10^{-4}$.

increase. To fix ideas, a map obtained with $\lambda = 10^{-3}$ in the case of Rayleigh waves will degrade to be comparable to the Love resolving radii map obtained with $\lambda = 10^{-4}$.

Another common way of accessing resolution is through checkerboard tests. We constructed synthetic earth models with equal-area cells of 10^6 and 4×10^6 square kilometres. To simulate an inversion of data corresponding to these models, it is sufficient to apply the resolution matrix to these models. The results for the Rayleigh case can be seen in Fig. 8. We clearly see that an average lateral resolution of about 1000 km can only be achieved in the Western Pacific and North America, whereas over the whole Earth we obtain an average lateral resolution of around 2000 km. This confirms what we have already seen from the resolving radii maps.

Resolving radii maps are a good means to represent the lateral resolution achievable in modern global surface-wave tomography. Checkerboard tests only show how well the particular chosen input checkerboard model is resolved. Strictly speaking, they do not say anything about any other input model, even for heterogeneity with a comparable wavelength. Resolving radii, on the other hand, provide a compact and more complete representation of the resolution operator.

5 DISCUSSION AND CONCLUSION

The methodology used in this paper is motivated by surface ray theory. In the *measurement* of mean-path phase velocities, the smoothing constraint is applied because the local dispersion relation along the path $c(\omega)$ is everywhere a smooth (analytic) function of frequency, and in ray theory the phase of the signal is given in terms of the integral of $\omega/c(\omega)$ along the ray-path. The measurements are expressed as mean phase-velocity anomalies (relative to the reference model); however it is important to note that it is, in fact, the anomaly in the phase of the signal that is measured. In a case where the wavefield was well described by ray theory, but the rays deviated greatly from the great-circle path, the measurements would nevertheless be valid. In the *interpretation* of the measurements, we have made the further assumption that Fermat's principle holds, i.e. that the measurements correspond to path integrals along the major- or minor-arc segments of the great-circle path. This could be relaxed in future work, and thus one could seek to interpret the same measurements in terms of laterally refracted rays, as has been done at very long periods by Wong (1989) and Pollitz (1994). The inversion, in this case, becomes non-linear, and the great-circle approximation employed here may be regarded as the first iteration of an iterative scheme. It is undoubtedly the case that there are many examples of off-great-circle propagation and non-ray-theoretical effects (e.g. Lay & Kanamori 1985; Woodhouse & Wong 1986; Snieder 1988; Levshin, Ratnikova & Berger 1992; Laske, Masters & Zürn 1994; Friederich *et al.* 1994). The extent to which such effects may corrupt the models constructed under the simple assumptions made here can be determined only by extensive

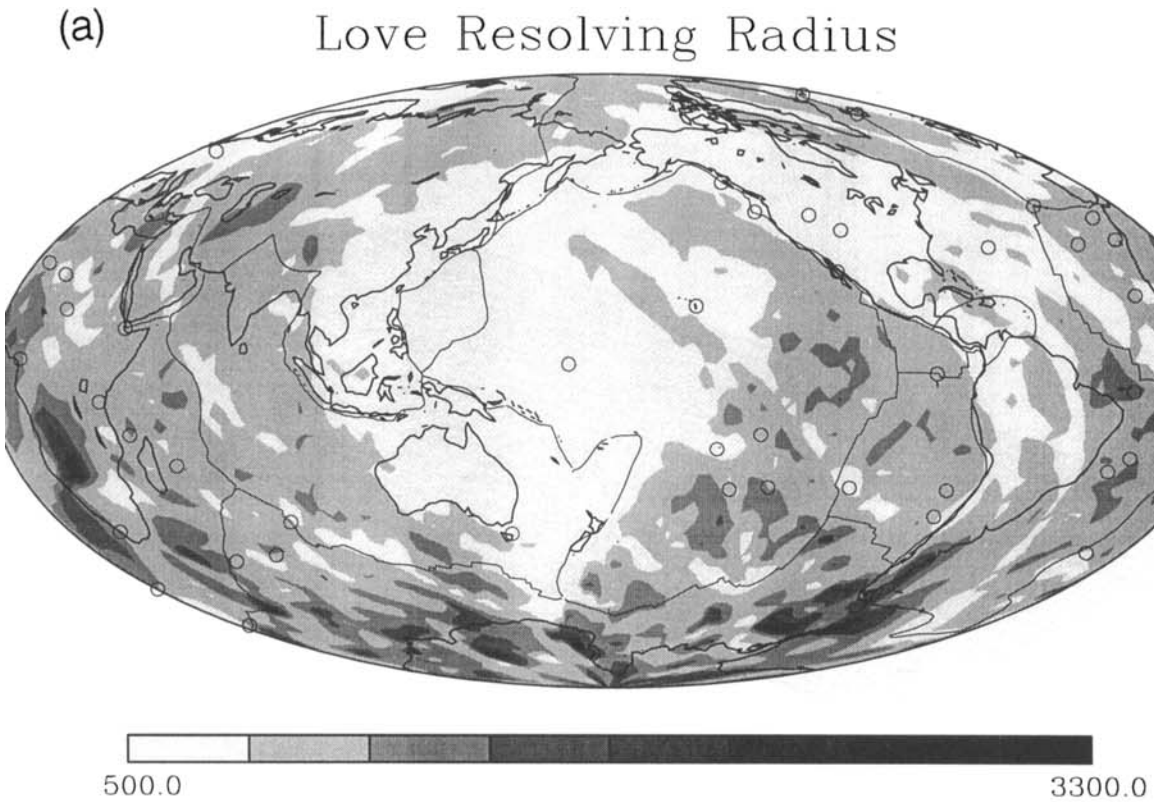

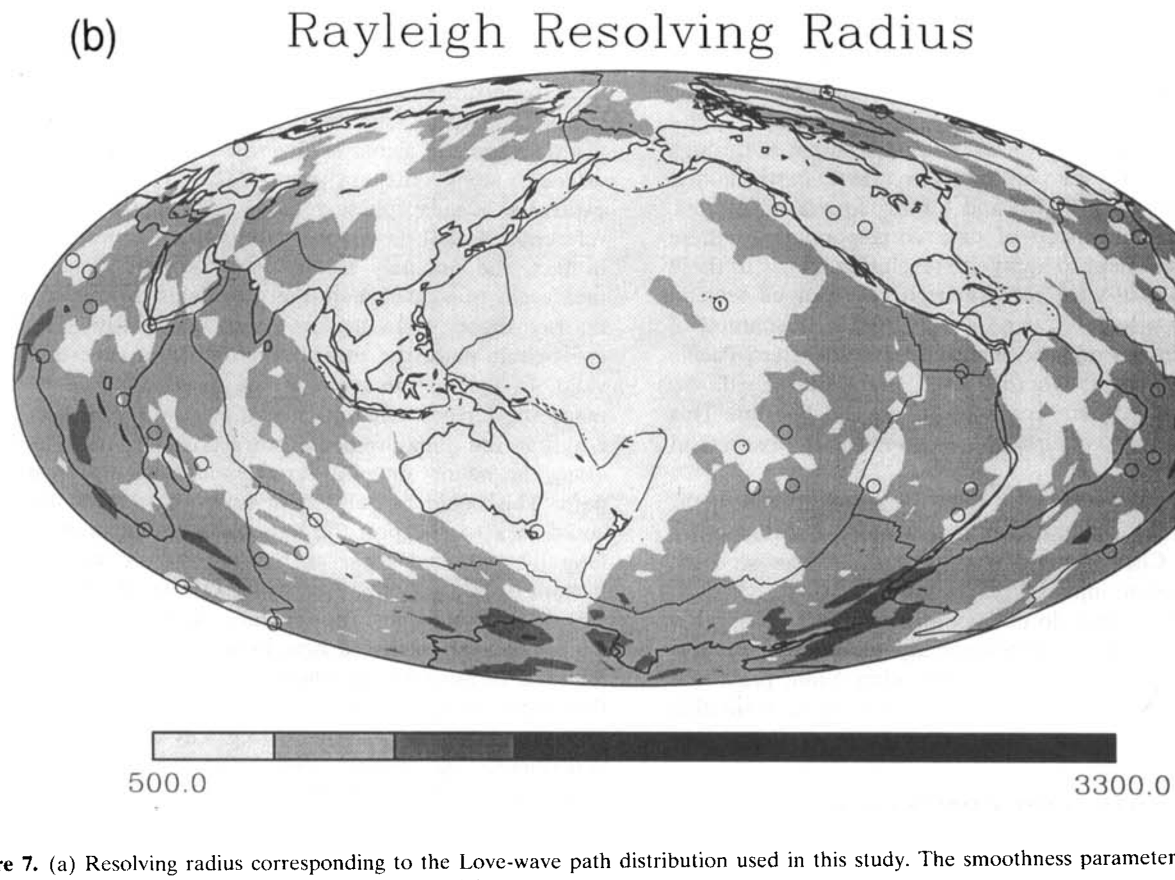

Figure 7. (a) Resolving radius corresponding to the Love-wave path distribution used in this study. The smoothness parameter $\lambda = 10^{-4}$ and the radii are given in km. (b) As for (a), but for Rayleigh waves.

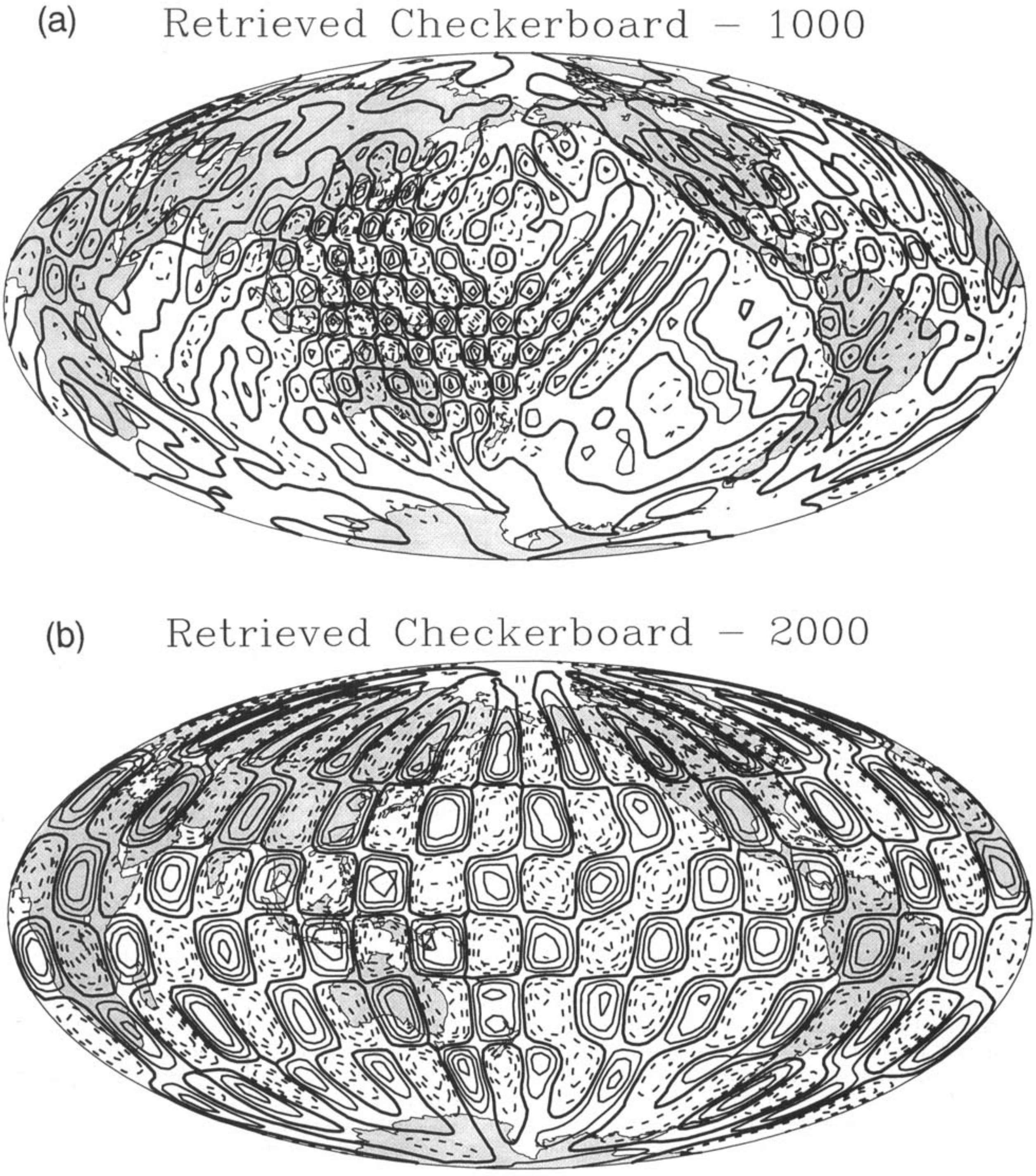

Figure 8. (a) Retrieved checkerboard for the Rayleigh-wave resolution with $\lambda = 10^{-4}$. The original checkerboard has been constructed with cells of approximately 10^6 square km of surface area. The amplitudes are relative to the input amplitude. The contour interval is 0.2: bold lines represent zero contours, dashed contours negative amplitudes and solid contours positive amplitudes. (b) As for (a), but for a surface area of 4×10^6 square km.

numerical simulations using more advanced algorithms for the construction of the theoretical seismograms. The issue is whether such effects enter as random noise to which the inversion is insensitive, or as a signal tending to bias or, indeed, to vitiate the results. Naturally, the frequency of occurrence and the magnitude of such effects (in general their statistics) are of importance, and will depend upon the spectrum of heterogeneity. We have not addressed these issues here. Instead we argue upon the basis of the large variance reduction, particularly at higher frequencies for which non-ray-theoretical effects are thought to be strongest, that a significant part of the signal, well described by ray theory, has been retrieved. The variance reduction at longer periods is lower, mainly, we believe, because the

Table 2. Correlation coefficients comparing our Love phase-velocity results with those predicted by M84A (Woodhouse & Dziewonski 1984). The correlation coefficients are given for each spherical harmonic degree, as well as for the total expansion (SH) and a pixel-based average described in the main text. Also shown are total data variance reductions.

Period	Variance	Correlation Coefficient									
	Reduction	D1	D2	D3	D4	D5	D6	D7	D8	SH	Pixel
39.982	86%	0.60	0.60	0.35	0.28	0.28	0.25	0.25	0.26	0.23	0.03
59.932	80%	0.38	0.76	0.56	0.57	0.61	0.60	0.59	0.58	0.56	0.37
79.689	71%	0.07	0.82	0.69	0.72	0.75	0.75	0.73	0.69	0.71	0.64
99.709	66%	0.41	0.85	0.75	0.79	0.80	0.80	0.77	0.72	0.75	0.73
150.919	53%	0.96	0.94	0.83	0.83	0.82	0.81	0.78	0.74	0.77	0.79

amplitude of heterogeneity in phase velocity is much smaller. Calculations by Woodhouse & Wong (1986) show that at long periods ($T \sim 150$ s) the effects of off-great-circle propagation are minor for the early orbits (R_1, R_2, G_1, G_2) used here, at least for the low-order models used in their study. The models derived here could be used as a starting point to estimate such effects at higher frequencies.

The most original feature of this study is the phase-velocity maps down to 40 s, much shorter periods than used in any other study to date. The Love-wave model at 40 s (Fig. 4a) shows a remarkable correlation with surface topography and bathymetry, and hence with crustal thickness. For Rayleigh waves (Fig. 5a), this resemblance is almost absent, but here the correlation is very good with certain tectonic features. This is to be expected: while Love waves at 40 s sample the surface, decaying exponentially with depth, Rayleigh-wave sampling is more complex with a maximum sensitivity at about 50 km depth, and hence Rayleigh waves have more sensitivity to upper-mantle structure. These maps are very stable, and together with the high data variance reduction (Tables 2 and 3) suggest that the great-circle approximation is quite robust up to these frequencies.

Considering longer periods, the waves are more and more sensitive to upper-mantle structure. The mid-oceanic ridges are the major low-velocity anomalies, together with regions characterized by back-arc volcanism. The Atlantic ridge is particularly well resolved for Love phase velocities (Figs 4b and c). High velocities are associated with continental shields and old ocean basins. Longer periods allow a comparison with previous studies. We note a good visual correlation of all major features between our models at 100 and 200 s and those obtained by Montagner & Tanimoto (1991) and Zhang & Tanimoto (1993).

At 150 s, our maps are in very good agreement with results obtained by Wong (1989) for both Love and Rayleigh waves. We made a more quantitative comparison between our phase-velocity maps and those predicted by M84A (Woodhouse & Dziewonski 1984). We calculated correlation coefficients for each spherical harmonic degree (1–8) as well as for all degrees taken together. Furthermore, we defined a pixel-based correlation coefficient, where we divided the earth into knots every 3 degrees in latitude and longitude. At each of those pixels, we calculated the corresponding phase velocity. The final correlation coefficient was then calculated for phase velocities at 7200 different points of the earth's surface. The results are shown in Tables 2 and 3. Figs 9(a) and (b) show the resemblance of Love-wave phase velocities at 150 s, corresponding to a correlation coefficient of 0.79. In general, the correlation is good at long periods, getting progressively worse at shorter periods. This is to be expected, as M84A was constructed using long periods. We find that the pixel-based correlation coefficient is more sensitive to visual resemblance than the total spherical harmonic one. Smith & Masters (1989) calculated spherical harmonic degree by degree correlations between their model, M84A and a model obtained by Davis (1987). The degree-by-degree correlation coefficients (Tables 2 and 3) with M84A indicate that our models at long periods are also similar to those obtained by Smith & Masters (1989), and hence to those by Davis (1987).

The spherical averages for Love phase velocities vary from 0.17 to 0.07 per cent with respect to PREM, corresponding to periods varying from 40 to 150 s. For Rayleigh phase velocities, they vary from 0.98 and 0.25 per cent for the same period interval. At long periods these results compare well with those obtained by Nakanishi & Anderson (1984) for instance. Total data variance

Table 3. As for Table 2, but for Rayleigh waves.

Period	Variance	Correlation Coefficient									
	Reduction	D1	D2	D3	D4	D5	D6	D7	D8	SH	Pixel
40.043	88%	0.12	0.60	0.48	0.51	0.56	0.55	0.56	0.54	0.53	0.44
60.147	82%	0.49	0.74	0.68	0.75	0.80	0.79	0.77	0.74	0.74	0.73
79.909	72%	0.74	0.78	0.74	0.83	0.85	0.85	0.81	0.77	0.80	0.80
100.393	60%	0.84	0.80	0.76	0.85	0.86	0.86	0.80	0.77	0.79	0.81
149.124	27%	0.90	0.85	0.75	0.85	0.83	0.81	0.71	0.68	0.73	0.73

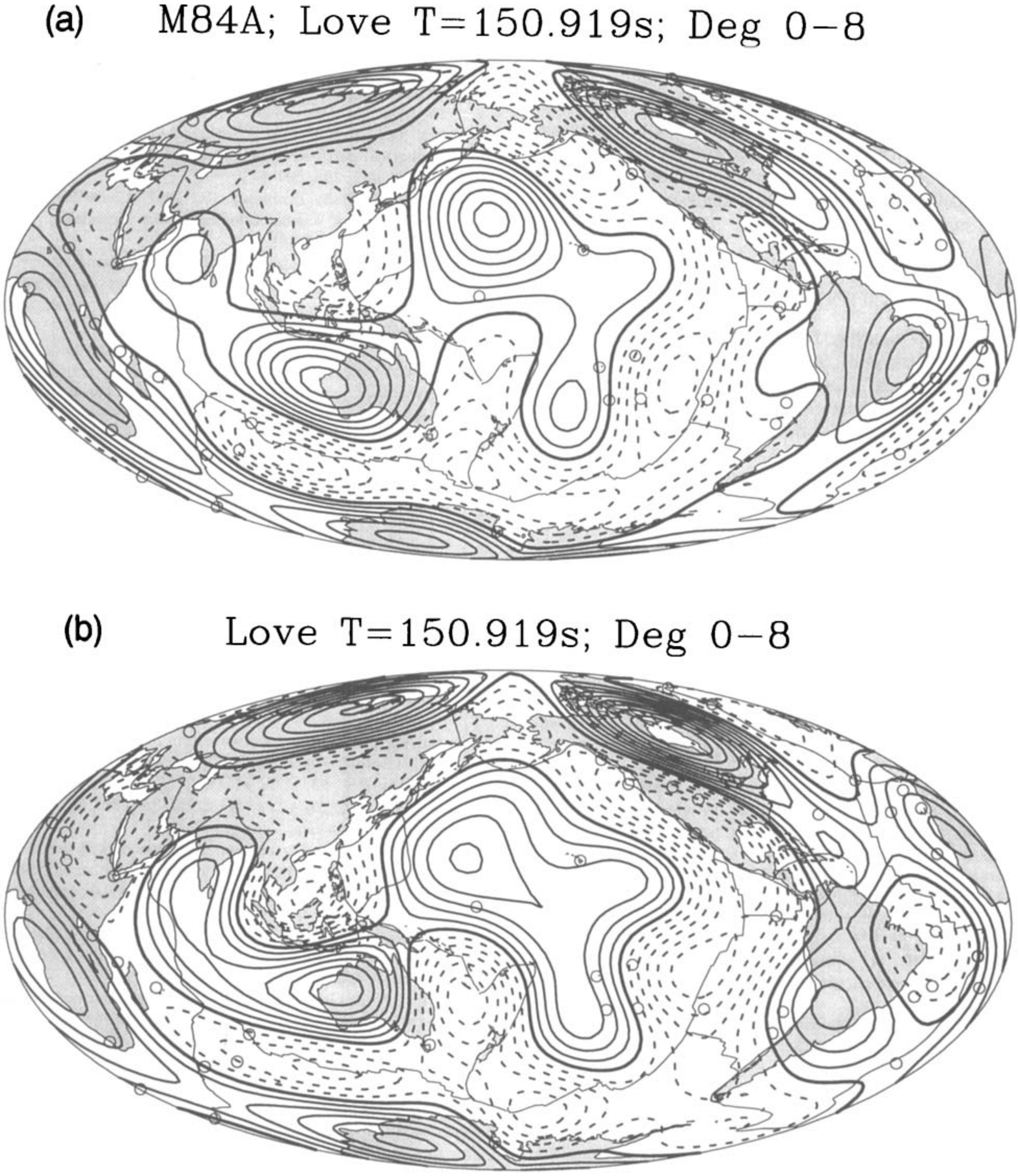

Figure 9. (a) Relative Love-wave phase velocity at 150 s predicted by M84A (Woodhouse & Dziewonski 1984) with a spherical harmonic expansion up to degree and order 8. The contour interval is 0.5 per cent: bold lines represent zero contours, dashed contours negative amplitudes and solid contours positive amplitudes. (b) As (a), but for our model.

reductions at long periods are comparable to those obtained by previous studies. The observed decrease in variance reduction with increasing period (Tables 2 and 3) is not due to different damping parameters, which only explains a few per cent. This behaviour is generally observed (e.g. Zhang & Tanimoto 1993), and, we believe, is a consequence of the fact that the heterogeneous signal—the departure from PREM—is much larger at shorter periods.

We obtained Love and Rayleigh phase-velocity maps between 40 and 150 s using a new method of waveform inversion for phase-velocity measurements. In the construction of the models, special care has been taken to avoid bias due to the truncation of the spherical harmonic expansion. The main result is that at 40 s, Love-wave phase velocities show a significant correlation with crustal structure, whereas Rayleigh phase velocities correlate better with tectonic features. The stability of the maps and the high data variance reduction suggest that the great-circle approximation is robust for the frequency range considered. At longer periods, our results are comparable with those of previous studies. Finally, a detailed resolution analysis shows that, for modern surface-wave tomography, the average lateral resolution is approximately 2000 km.

ACKNOWLEDGMENTS

This work was done while JT was supported by a fellowship from the Commission of the European Communities in the framework of the SCIENCE program. We wish to thank Andy Jackson for numerous discussions and routines involving B-splines. Special thanks go to all those involved in collecting and distributing the high-quality GDSN and GEOSCOPE data.

REFERENCES

Backus, G.E. & Gilbert, J.F., 1968. The resolving power of gross earth data, *Geophys. J. R. astr. Soc.*, **16**, 169–205.

Brune, J.N., 1969. Surface Waves and Crustal Structure, in *The Earth's Crust and Upper Mantle*, ed. Pembroke, P.J., Geophys. Mono. Am. Geophys. Un., **13**, 230–242.

Cara, M., 1973. Filtering of dispersed wavetrains, *Geophys. J. R. astr. Soc.*, **33**, 65–80.

Constable, C.G. & Parker, R.L., 1988. Smoothing, splines and smoothing splines; their application in Geomagnetism, *J. Comput. Phys.*, **78**, 493–508.

Davis, J.P., 1987. Local eigenfrequency and its uncertainty inferred from spheroidal mode frequency shifts, *Geophys. J. R. astr. Soc.*, **88**, 693–722.

Dorman, J., 1969. Seismic Surface-Wave Data on the Upper Mantle, in *The Earth's Crust and Upper Mantle* (ed. Pembroke, P.J.), Geophys. Mono., Am. Geophys. Un., **13**, 257–265.

Dziewonski, A.M. & Anderson, D.L., 1981. Preliminary Reference Earth Model, *Phys. Earth planet. Inter.*, **25**, 297–356.

Dziewonski, A.M. & Woodhouse, J.H., 1982. Analysis of earthquake source parameters from digital data, *Terra Cognita*, **2**, 176–177.

Dziewonski, A.M. & Woodhouse, J.H., 1983. Studies of the seismic source using normal mode theory, *Proc. Enrico Fermi Int. Sch. Phys., LXXXV*, pp. 45–137, eds Kanamori, H.R. & Boschi, E., Nioza, Amsterdam.

Edmonds, A.R., 1960. *Angular Momentum and Quantum Mechanics*, Princeton Univ. Press, Princeton, NJ.

Friederich, W., Wieland, E. & Stange, S., 1994. Non-plane geometries of seismic surface wave fields and their implications for regional-scale surface wave tomography, *Geophys. J. Int.*, **119**, 931–948.

Gilbert, F., 1971. Excitation of normal modes of the Earth by earthquake sources, *Geophys. J. R. astr. Soc.*, **22**, 223–226.

Gutenberg, B., 1924. Dispersion und Extinktion von seismischen Oberfächenwellen und der Aufbau der obersten Erdschichten, *Physikalische Zeitschrift*, **25**, 377–382.

Lancaster, P. & Salkauskas, K., 1986. *Curve and Surface Fitting: An Introduction*, Academic Press, London.

Laske, G., Masters, G. & Zürn, W., 1994. Frequency-dependent polarization measurements of long-period surface waves and their implications for global phase velocity maps, *Phys. Earth planet. Inter.*, **84**, 111–137.

Lay, T. & Kanamori, H., 1985. Geometric effects of global lateral heterogeneity on long-period surface wave propagation, *J. geophys. Res.*, **90**, 605–621.

Levshin, A., Ratnikova, L. & Berger, J., 1992. Pecularities of surface-wave propagation across central Eurasia, *Bull. seism. Soc. Am.*, **82**, 2464–2493.

Masters, G., Jordan, T.H., Silver, P.G. & Gilbert, F., 1982. Aspherical earth structure from fundamental spheroidal mode data, *Nature*, **298**, 609–613.

Montagner, J.-P. & Tanimoto, T., 1991. Global upper mantle tomography of seismic velocities and anisotropies, *J. geophys. Res.*, **96**, 20 337–20 351.

Nakanishi, I. & Anderson, D.L., 1982. Worldwide distribution of group velocity of mantle Rayleigh waves as determined by spherical harmonic inversion, *Bull. seism. Soc. Am.*, **72**, 1185–1194.

Nakanishi, I. & Anderson, D.L., 1983. Measurement of mantle wave velocities and inversion for lateral heterogeneity and anisotropy, I. Analysis of great circle phase velocities, *J. geophys. Res.*, **88**, 10 267–10 283.

Nakanishi, I. & Anderson, D.L., 1984. Measurement of mantle wave velocities and inversion for lateral heterogeneity and anisotropy, II. Analysis by the single station method, *Geophys. J. R. astr. Soc.*, **78**, 573–618.

Parker, R.L., 1994. *Geophysical Inverse Theory*, Princeton Univ. Press, Princeton, NJ.

Pollitz, F.F., 1994. Global tomography from Rayleigh and Love wave dispersion; effect of ray-path bending, *Geophys. J. Int.*, **118**, 730–758.

Shure, L., Parker, R.L. & Backus, G.E., 1982. Harmonic splines for geomagnetic modelling, *Phys. Earth planet. Inter.*, **28**, 215–229.

Smith, M.F. & Masters, G., 1989. Aspherical structure constraints from free oscillation frequency and attenuation measurements, *J. geophys. Res.*, **94**, 1953–1976.

Snieder, R., 1988. Large scale waveform inversions of surface waves for lateral heterogeneity, 1. Theory and numerical examples, *J. geophys. Res.*, **93**, 12 055–12 065.

Stacey, F.D., 1992. *Physics of the Earth*, 3rd edn., Brookfield Press, Brisbane, Australia.

Tams, E., 1921. Über Fortplanzungsgeschwindigkeit der seismischen Oberflächenwellen längs kontinentaler und ozeanischer Wege, *Centralblatt für Mineralogie, Geologie und Paläontologie*, **2–3**, 44–52.

Tarantola, A. & Valette, B., 1982. Generalized non-linear inverse problems solved using the least squares criterion, *Rev. Geophys. Space Phys.*, **20**, 219–232.

Whaler, K.A. & Gubbins, D., 1981. Spherical harmonic analysis of the geomagnetic field: An example of a linear inverse problem, *Geophys. J. R. astr. Soc.*, **65**, 645–693.

Wong, Y.K., 1989. Upper mantle heterogeneity from phase and amplitude data of mantle waves, *PhD thesis*, Harvard Univ., Cambridge, MA.

Woodhouse, J.H. & Dziewonski, A.M., 1984. Mapping the upper mantle: Three dimensional modelling of Earth structure by inversion of seismic waveforms, *J. geophys. Res.*, **89**, 5953–5986.

Woodhouse, J.H. & Wong, Y.K., 1986. Amplitude, phase and path anomalies of mantle waves, *Geophys. J. R. astr. Soc.*, **87**, 753–773.

Zhang, Y.-S. & Tanimoto, T., 1993. High-resolution global upper mantle structure and plate tectonics, *J. geophys. Res.*, **98**, 9739–9823.

APPENDIX A

The models are specified in terms of the normalized, real spherical harmonics commonly used in representing the geoid (e.g. Stacey 1992). Writing

$$p_l^m(\theta) = \left[(2-\delta_{m,0})(2l+1)\frac{(l-m)}{(l+m)}\right]^{1/2} P_l^m(\cos\theta), \tag{A1}$$

where $P_l^m(\cos\theta)$ are the associated Legendre polynomials, the relative phase-velocity perturbation is given by

$$\frac{\delta c}{c} = \sum_{l=0}^{L}\sum_{m=0}^{l}(A_l^m \cos m\varphi + B_l^m \sin m\varphi)p_l^m(\theta). \tag{A2}$$

The coefficients A and B are those listed in Tables A1 and

Table A1. Spherical harmonic coefficients, multiplied by 10 000, corresponding to the relative Love-wave phase-velocity model at 39.982 s.

l	m	A	B	l	m	A	B	l	m	A	B	l	m	A	B
0	0	17.39			3	2.91	3.17		11	2.92	4.27		3	-6.55	-12.49
1	0	-65.51			4	9.83	13.61		12	-3.04	4.73		4	8.68	-5.85
	1	-38.46	-22.03		5	3.53	-21.59		13	-5.46	7.24		5	-4.15	-3.40
2	0	-39.86			6	12.11	3.84		14	-3.81	3.74		6	6.13	6.13
	1	-43.16	-58.87		7	5.57	8.45	15	0	-11.54			7	-0.27	-7.45
	2	72.22	11.14		8	-11.91	25.57		1	-9.14	0.64		8	-4.12	1.76
3	0	6.94			9	-13.35	20.47		2	-7.80	-5.38		9	2.25	3.10
	1	22.78	-16.01		10	-25.50	5.35		3	-11.24	0.39		10	-0.63	2.57
	2	42.10	-47.13	11	0	14.92			4	-0.28	11.70		11	9.01	-8.77
	3	-38.01	-73.49		1	-9.26	-9.90		5	5.35	0.03		12	-7.27	0.67
4	0	-19.22			2	-10.11	6.94		6	-12.87	9.80		13	-1.92	9.93
	1	24.34	9.54		3	8.46	7.01		7	-6.41	-9.22		14	-6.12	4.81
	2	18.12	-16.43		4	6.62	4.21		8	3.57	-7.36		15	-7.65	6.65
	3	-48.90	7.62		5	-15.94	-4.28		9	-1.09	-3.92		16	-1.94	-8.67
	4	10.88	-27.52		6	-7.41	-5.27		10	-0.88	-3.90		17	-4.54	2.17
5	0	41.46			7	8.47	14.97		11	-0.46	3.19		18	-2.93	-1.38
	1	23.23	10.50		8	-7.88	-12.07		12	10.67	-2.19	19	0	-2.05	
	2	-13.10	8.34		9	13.62	-14.62		13	8.24	6.14		1	3.40	-2.03
	3	-22.66	-6.24		10	1.74	-3.26		14	-1.31	5.35		2	5.52	-5.73
	4	-23.04	-25.88		11	-9.00	-2.51		15	-5.86	-0.31		3	-4.72	-6.29
	5	14.21	-13.00	12	0	-7.38		16	0	4.69			4	2.59	-0.54
6	0	-7.04			1	12.87	10.57		1	1.88	8.67		5	-5.17	-2.16
	1	-12.38	-14.13		2	21.80	2.51		2	-3.27	0.94		6	-0.74	2.61
	2	-8.69	25.99		3	-13.27	10.77		3	14.17	8.86		7	-1.40	1.17
	3	-8.32	-16.65		4	3.21	5.61		4	-0.55	1.30		8	4.86	-3.10
	4	-19.16	14.52		5	10.09	12.48		5	-7.02	10.87		9	3.36	-0.36
	5	32.22	28.06		6	3.39	-9.04		6	-7.48	6.23		10	-1.07	-2.78
	6	-16.28	-11.79		7	10.76	10.66		7	-4.69	5.66		11	6.84	-1.05
7	0	14.72			8	2.09	-9.14		8	-0.62	-8.71		12	-3.61	6.10
	1	-3.46	-17.04		9	-11.52	1.32		9	5.86	7.01		13	-3.43	2.39
	2	-5.89	-4.13		10	-13.69	6.44		10	2.40	7.00		14	-2.90	-7.02
	3	-4.09	13.93		11	2.28	5.44		11	5.83	-4.95		15	7.16	-1.51
	4	31.84	-1.50		12	-0.96	3.67		12	-7.59	1.97		16	6.69	-1.77
	5	7.44	-3.65	13	0	4.97			13	-7.92	7.83		17	-3.09	6.61
	6	5.37	13.90		1	4.26	-8.89		14	-2.29	6.91		18	-3.75	4.05
	7	-1.42	13.07		2	4.29	14.20		15	-18.82	-0.47		19	7.31	0.30
8	0	-7.36			3	11.81	-14.31		16	6.51	8.67	20	0	0.55	
	1	-5.83	-1.14		4	2.38	-6.44	17	0	7.00			1	1.01	4.24
	2	-21.99	-13.25		5	-6.30	15.62		1	7.78	11.20		2	6.26	-0.24
	3	9.69	-6.82		6	1.68	13.28		2	2.65	9.30		3	-0.80	-2.11
	4	-3.75	-11.07		7	2.95	23.67		3	-16.08	-13.26		4	0.74	-0.18
	5	21.48	-1.21		8	-0.01	-13.45		4	-6.34	9.37		5	2.91	1.17
	6	7.93	-11.90		9	-2.96	-13.91		5	8.65	-9.87		6	-2.03	-7.88
	7	-20.86	-10.76		10	6.04	3.39		6	0.38	-6.23		7	5.55	1.61
	8	7.37	22.82		11	11.56	-1.53		7	0.67	-1.03		8	0.45	-3.92
9	0	19.33			12	32.51	-7.21		8	-0.25	-6.07		9	-0.08	4.45
	1	-10.53	-18.58		13	-0.07	-10.34		9	6.87	13.36		10	-0.35	-0.57
	2	-6.57	-3.32	14	0	11.65			10	5.08	-11.99		11	-0.90	-0.87
	3	31.74	9.44		1	-0.85	9.97		11	7.68	-6.68		12	7.13	2.86
	4	2.91	-12.21		2	13.68	14.19		12	-2.86	-0.16		13	-0.52	0.22
	5	-8.66	0.94		3	-6.20	3.51		13	-6.14	11.64		14	0.30	-1.88
	6	-2.59	-18.22		4	-9.88	8.49		14	-3.92	1.76		15	5.34	0.05
	7	3.19	18.15		5	9.15	-2.31		15	5.01	-8.86		16	3.13	-1.12
	8	-27.00	-21.66		6	-3.13	-8.89		16	13.05	-9.93		17	-1.29	-4.27
	9	10.32	11.35		7	-5.38	9.54		17	-2.60	6.98		18	-0.51	0.35
10	0	10.52			8	-2.63	-1.25	18	0	-0.78			19	2.56	-2.16
	1	4.01	7.36		9	2.99	-10.42		1	4.16	7.21		20	3.45	7.96
	2	19.14	2.52		10	-4.62	-1.25		2	-3.98	3.39				

Table A2. As for Table A1, but for Rayleigh waves at 40.043 s.

l	m	A	B	l	m	A	B	l	m	A	B	l	m	A	B
0	0	98.15			3	-12.79	5.92		11	-2.22	13.04		3	0.77	-4.86
1	0	-19.33			4	2.74	3.72		12	0.40	-5.19		4	6.72	-9.84
	1	-4.22	-14.89		5	0.87	-4.07		13	-3.48	1.79		5	6.28	0.45
2	0	-16.69			6	13.24	6.17		14	6.36	9.86		6	1.13	-1.33
	1	-29.24	-48.28		7	2.58	-7.69	15	0	-3.78			7	-1.27	-2.56
	2	64.45	0.16		8	-13.26	0.77		1	1.26	3.82		8	-5.45	-3.39
3	0	11.90			9	-5.93	-2.40		2	-4.24	-2.62		9	2.68	4.39
	1	19.35	-16.66		10	-22.18	10.46		3	-9.52	-7.05		10	-5.05	0.27
	2	11.87	-22.92	11	0	11.68			4	7.72	0.67		11	1.34	-2.13
	3	-35.54	-48.02		1	-11.93	-2.17		5	-4.32	2.59		12	-5.24	3.70
4	0	-1.31			2	-1.41	-4.08		6	-7.37	3.56		13	1.57	12.45
	1	19.23	9.20		3	14.92	2.12		7	-4.54	-11.46		14	2.10	-7.12
	2	-3.56	-6.51		4	1.06	5.35		8	-0.18	-9.22		15	-0.46	3.64
	3	-38.88	-0.05		5	-3.89	-17.54		9	6.32	-5.80		16	-0.76	0.03
	4	1.10	0.33		6	1.71	-1.25		10	-8.37	-7.20		17	0.62	-0.92
5	0	12.14			7	12.25	16.68		11	-1.43	2.40		18	1.23	-4.33
	1	28.77	10.72		8	-10.13	-5.55		12	4.06	-10.62	19	0	-0.78	
	2	-37.50	5.38		9	8.41	-16.87		13	2.20	-6.29		1	-1.75	6.08
	3	-15.09	5.66		10	0.75	4.78		14	-6.99	-1.49		2	-0.15	2.81
	4	11.29	-34.95		11	5.18	-10.95		15	1.21	-0.37		3	2.73	-9.94
	5	17.16	6.74	12	0	2.70		16	0	5.57			4	-0.15	-1.17
6	0	1.78			1	14.58	-1.70		1	-4.10	-2.63		5	-3.06	0.84
	1	-5.10	-11.62		2	6.90	-8.33		2	-0.89	-4.61		6	8.81	-6.97
	2	-16.17	27.84		3	-4.90	8.60		3	2.86	8.39		7	2.59	0.84
	3	2.20	-3.21		4	-1.63	5.60		4	-0.42	-1.15		8	1.18	4.20
	4	-5.81	12.37		5	-3.41	12.09		5	-5.00	-0.57		9	-7.41	-3.74
	5	26.53	26.35		6	-2.64	3.17		6	-3.12	4.12		10	1.83	-5.30
	6	-5.71	-5.35		7	-1.24	-2.97		7	1.39	-1.40		11	-3.25	-2.23
7	0	-3.70			8	2.77	-4.62		8	-1.59	-1.87		12	-0.97	1.95
	1	-5.34	14.41		9	-7.90	-2.00		9	7.64	7.29		13	-1.96	2.23
	2	-3.49	-3.40		10	-9.34	3.61		10	-1.05	3.64		14	-2.66	1.12
	3	-8.71	16.36		11	-9.10	-7.58		11	3.38	-5.16		15	8.49	2.28
	4	8.77	17.63		12	-13.57	-8.03		12	-4.31	-2.21		16	-6.78	1.51
	5	9.65	-20.91	13	0	-2.15			13	-4.44	3.52		17	-2.27	6.84
	6	12.33	-18.23		1	9.07	-2.54		14	9.10	5.90		18	-7.93	2.35
	7	1.95	1.66		2	3.54	11.54		15	-8.29	8.96		19	3.86	2.95
8	0	-9.37			3	6.73	-8.89		16	1.58	2.50	20	0	0.15	
	1	-8.10	-3.72		4	3.59	-0.04	17	0	1.63			1	-1.86	1.66
	2	-17.88	0.05		5	-6.80	6.79		1	4.58	1.49		2	0.04	-1.88
	3	-2.05	0.93		6	6.58	-0.98		2	3.43	-2.01		3	-0.13	-2.47
	4	14.52	-10.59		7	4.46	23.31		3	-8.20	-1.49		4	-1.73	3.90
	5	-3.02	-4.33		8	-2.22	-3.45		4	-4.20	2.39		5	-5.80	2.42
	6	-6.37	-3.66		9	-5.89	-9.68		5	6.18	-2.06		6	-2.37	2.82
	7	-27.37	-5.76		10	-4.06	3.43		6	-2.20	-10.12		7	2.65	3.86
	8	13.46	6.20		11	-1.76	4.77		7	-2.99	-3.18		8	4.62	1.30
9	0	3.04			12	12.55	-5.46		8	-5.27	0.03		9	-1.94	1.10
	1	-12.22	-18.84		13	3.92	-11.07		9	10.08	10.97		10	-0.66	-1.42
	2	-12.62	1.93	14	0	0.20			10	3.54	-3.43		11	-2.25	-2.84
	3	29.05	4.63		1	1.75	-6.05		11	1.87	-12.47		12	-1.54	-1.53
	4	1.93	-5.22		2	9.67	9.44		12	-5.95	0.79		13	-5.45	2.29
	5	-6.64	-1.74		3	-3.33	-1.15		13	-4.30	0.23		14	-1.35	-1.03
	6	-8.76	-14.53		4	-10.48	0.77		14	2.34	9.93		15	7.35	-0.88
	7	10.93	25.42		5	1.56	7.35		15	9.08	-1.07		16	1.16	2.09
	8	-12.48	-13.01		6	4.05	-6.83		16	10.92	-13.07		17	3.45	0.82
	9	1.20	0.42		7	-2.33	-2.41		17	8.39	11.30		18	-5.07	5.68
10	0	-1.67			8	-2.51	-11.03	18	0	4.99			19	2.59	-2.81
	1	-2.02	2.34		9	-5.42	-6.96		1	-0.09	4.19		20	-4.38	-1.51
	2	5.10	-5.22		10	-3.17	7.50		2	-5.35	1.65				

A2 up to degree and order 20, which corresponds to the average lateral resolution achieved in this study. Coefficients up to degree and order 40 for all models are available on request by e-mail from jeannot@sismo.u-strasbg.fr or john@earth.ox.ac.uk.